Synchronous enhancement of mechanical properties and degradation rates of as-extruded Mg−Er−Ni alloys by controlling Er content

Chao-neng DAI[1,2], San-lue PEI[2], Ye WANG[2], Zi-hong WANG[2], Jin-xing WANG[2], Yan-long MA[3], Jing-feng WANG[1,2]

1. College of Chemistry and Chemical Engineering, Chongqing University, Chongqing 401331, China;
2. National Engineering Research Center for Magnesium Alloys, College of Materials Science and Engineering, Chongqing University, Chongqing 400044, China;
3. College of Materials Science and Engineering, Chongqing University of Technology, Chongqing 400054, China

Abstract: The synchronous enhancement mechanism of the mechanical properties and degradation rate of as-extruded Mg−xEr−1.6Ni alloys (x=17, 12, and 9.5, wt.%) was investigated by controlling Er content. Results indicate that, as the Er content decreases, the overall content and the distribution of secondary phases did not change evidently, while the type of the secondary phases changed from single long-period stacking ordered (LPSO) phase to coexistence of the LPSO phase and γ' phase. Notably, the tensile yield strength (TYS) and degradation rate of the Mg alloy with a lower Er content (i.e., Mg−9.5Er−1.6Ni alloy) are increased by 22.3% and 51.5% respectively compared to those of the Mg alloy with a higher Er content (i.e., Mg−17Er−1.6Ni). The enhancement of mechanical properties of the Mg alloy with a lower Er content is attributed to the formation of γ' phase, which can refine the grain size by inhibiting dynamic recrystallization, leading to enhanced TYS by secondary phase and grain boundary strengthening. Meanwhile, finer grains and the γ' phase also provide more corrosion sites and inhibit the formation of corrosion-resistant Er_2O_3 film, thereby accelerating the corrosion of Mg alloy.

Key words: Mg−Er−Ni alloy; mechanical properties; degradation rate; γ' phase

1 Introduction

Soluble magnesium (Mg) alloys, which are recognized for their low density, high specific strength, and limited corrosion resistance, have garnered significant research attention. They are particularly prominent in the development of key fracturing tools for the extraction of unconventional oil and gas resources, aiming to enhance production and well efficiency [1−4]. However, the challenge lies in the designing soluble Mg alloys that exhibit both high strength and rapid degradation rate, which are suitable for application in extreme exploitation environments characterized by elevated pressure and temperature conditions, such as deep downhole operations [5]. Thus, it is crucial to conduct further investigation to explore methods for fabricating advanced Mg alloys that can simultaneously enhance strength and degradation rate.

In the pursuit of high-strength and rapid-degradation Mg alloys, rare earth (RE) and transition metal (TM) elements, such as Cu and Ni, are commonly explored. The long-period stacking ordered (LPSO) phase, composed of Mg, rare earth elements (Gd, Y, Er, Dy), and transition metal elements (Ni, Cu), is recognized as an effective secondary phase for enhancing both the mechanical strength and degradation properties of soluble Mg

alloys. ZHANG et al [6] discovered that the mechanical performance of Mg96Er3Ni1 (at.%) alloy exceeded that of Mg96Er3Cu1 (at.%) alloy. Therefore, Mg−RE−Ni alloys containing the Ni-LPSO phase show great potential in developing materials with both high strength and degradation rate.

Considerable researches have focused on investigating the influence of the Ni-LPSO phase on the mechanical and degradation properties of alloys [7−11]. In our previous study, we explored Mg−Y−Ni alloys with varied contents of the Ni-LPSO phase by adjusting the contents of Y and Ni. The investigation revealed an improvement in mechanical properties with increasing content of the Ni-LPSO phase, while degradation properties exhibited an inverse trend. This divergence is stemmed from the dual effects of secondary phase strengthening and the corrosion barrier offered by the Ni-LPSO phase with high volume fraction. Although the introduction of the Ni-LPSO phase enhances the mechanical properties of Mg−RE−Ni alloys, an inherent trade-off exists between the high mechanical properties and rapid degradation rate, thereby limiting the overall properties of Mg−RE−Ni alloys.

Previous studies on binary Mg−Er, Mg−Y, and Mg−Gd alloys in biomedical applications revealed that Mg−Er alloys exhibited higher yield strength compared to the other two alloys. This distinction may be attributed to the larger atomic radius of Er (245 pm) and the more pronounced effect on solid-solution strengthening [12]. Additionally, Mg−Er alloys had shown higher corrosion current density and increased susceptibility to corrosion compared to other Mg−RE alloys. This susceptibility might be attributed to the fact that the corrosion product layer on Mg−Er alloys tends to peel off easily, allowing penetration of Cl⁻ ions and therefore corrosion attack. Consequently, alloying Mg with Er has the potential for synergistically enhancing the mechanical and degradation properties. Moreover, it has been noted that the Ni-LPSO phase can be formed in Mg−Er− Ni alloys [6,13]. However, the influence of Er content on the LPSO phase, microstructure distribution, and mechanical and degradation properties remains unclear.

This study involved preparation of as-extruded Mg−Er−Ni alloys containing Ni-LPSO phase by varying the content of Er, while maintaining a constant content of Ni. A comprehensive investigation was undertaken to elucidate the underlying mechanisms for the enhancement of the mechanical and degradation properties. This research not only contributes to the development and design of high-strength, high-degradation alloys but also offers significant insights into the intrinsic mechanisms governing the interplay between mechanical and degradation properties, particularly in alloys within the soluble Mg alloy field.

2 Experimental

2.1 Preparation of material

In a resistance furnace shielded with CO_2 and SF_6 gas at 750 °C, master alloys comprising pure Mg (99.97 wt.%), Mg−20.28Er (wt.%), and Mg−26.18Ni (wt.%) were employed to prepare Mg−xEr−1.6Ni alloys (x=17, 12, and 9.5, wt.%). The detailed compositions were listed in our prior work [8]. The melt was swirled for 2 min after melting, kept for 30 min, and then the crucible containing the melt was cooled in brine quickly to obtain a Mg−Er−Ni ingot with a diameter of 85 mm. Subsequently, the ingot with a diameter of 80 mm was extruded at an extrusion temperature of 400 °C and an extrusion ratio of 11 to obtain Mg−Er−Ni bar with a diameter of 25 mm. The as-extruded Mg−xEr−1.6Ni (wt.%) alloys were designated EM17EN, EM12EN, and EM9EN with a content of Er from high to low, respectively.

2.2 Characterization of materials

The secondary phase in the alloy was characterized using the Zeiss Libra 200 FE-TEM transmission electron microscope (TEM) and Rigaku D/Max2500PC X-ray diffraction (XRD). Samples were initially ground to a thickness of 40−50 μm using SiC emery paper and then thinned to less than 100 nm for TEM analysis via Gatan 695 low-temperature ion milling. The characterization of corrosion products was performed using X-ray diffraction (XRD, Rigaku D/Max2500PC) and X-ray photoelectron spectroscopy (XPS, Thermo Scientific K-Alpha) with a pressure of $5×10^{-7}$ Pa, an energy of 20 eV per pass, and a spot size of 400 μm. The texture, average grain size (AGS), and orientation of the as-extruded sample were analyzed

using a field-emission scanning electron microscope (FE-SEM; JEOL JSM−7800F) with an electron backscattered diffraction (EBSD) system (HKL Chanel 5). The analysis was performed with a step size of 0.45 mm. The mechanical properties along the extrusion direction were evaluated using dog-bone samples on a Shimadzu CMT−5105 testing machine with a strain rate of 2 mm/min.

2.3 Immersion test

Before hydrogen evolution and weight loss tests, all samples were ground using SiC sandpaper with grit sizes ranging from 400# to 2000#. These tests were conducted in a 3 wt.% KCl solution at temperatures of (25±1) and (93±1) °C, respectively. The as-extruded sample was cut into a $d10$ mm × 5 mm shape, embedded in resin, with only one side exposed for testing. The hydrogen evolution test was conducted at 25 °C in a 3 wt.% KCl solution and measured using the drainage method, and the volume of evolved-hydrogen was recorded every 10 min for a total test duration of 90 min for three sets. After the immersion test, the corrosion samples were cleaned in a solution containing 200 g/L CrO_3 + 10 g/L $AgNO_3$ for 10 min to remove the corrosion products. The formulas for hydrogen evolution volume (HEV), mass loss corrosion rate (MLR), and hydrogen evolution rate (HER) were provided by our previous studies [5,11].

2.4 Electrochemical measurements

Electrochemical impedance spectroscopy (EIS), potentiodynamic polarization, and polarization resistance measurements were conducted using a Gamry Interface 1010E electrochemical workstation in a 70 mL 3 wt.% KCl electrolyte at room temperature. The experimental setup comprised a three-electrode system, with a platinum sheet serving as the counter electrode, the working electrode consisting of the as-extruded Mg−xEr−1.6Ni alloy with a 1 cm² exposed surface area, and a saturated calomel reference electrode. Before conducting the EIS and potentiodynamic polarization tests, a 10 min measurement of open circuit potential (OCP) was performed to stabilize the electrochemical reaction. The EIS test was performed across a frequency range from 100 kHz to 10 mHz with a perturbation amplitude of 10 mV at an acquisition rate of 5 points/decade. Corrosion current density (J_{corr}) and corrosion potential (φ_{corr})

were derived from potentiodynamic polarization measurements at a scanning rate of 3 mV/s. Furthermore, polarization resistance was measured at a scanning rate of 1 mV/s within the potential range from −0.02 to 0.02 V.

3 Results

3.1 Microstructures of as-extruded Mg−xEr−1.6Ni alloy

The OM images and backscattered electron (BSE) micrographs presented in Fig. 1 show the microstructure distribution and phase composition of the as-extruded Mg−Er−Ni alloy. Reducing Er content from 17 wt.% to 9.5 wt.% induced dynamic recrystallization, as evidenced by the presence of dynamically recrystallized (DRXed) grains (Figs. 1(a, d, g)). A noticeable refinement in recrystallized grains was observed with decreasing Er content, which was particularly pronounced in the EM9EN alloy. The alloy exhibited a streamlined distribution of the secondary phase elongated along the extrusion direction (Figs. 1(b, e, h)). Composition analysis confirmed a predominant presence of an LPSO phase composed of Mg, Er, and Ni, which was validated by EDS results displaying an appropriate Er and Ni atomic ratio (Figs. 1(c, f, i)) [14]. Furthermore, the EM9EN alloy with lower Er content exhibited lamellar structured phases within the Mg matrix, potentially corresponding to the γ' phase as reported in previous studies [8].

Figure 2 illustrates the XRD patterns of the as-extruded alloy with both the full spectrum and an enlarged view. Comparison with standard cards of Mg (35-0821#) and the LPSO phase (36-1273#), the phase constitutions were predominantly the LPSO phase and Mg matrix, which aligned with SEM results. Notably, the XRD peak spectrum in 2θ range of 20°−50° indicated a predominant alignment of the Mg matrix along the (0002) basal plane. The similar intensities of diffraction peaks observed for the LPSO phase suggested minimal variations within the alloys. Specifically, the alloys with a high content of Er exhibited overlapping diffraction peaks of the Mg matrix, whereas in the EM9EN alloy, all peaks shifted to lower angles. This shift implied an expanded lattice constant and interplanar spacing in the Mg matrix, potentially associated with the formation of lamellar phases.
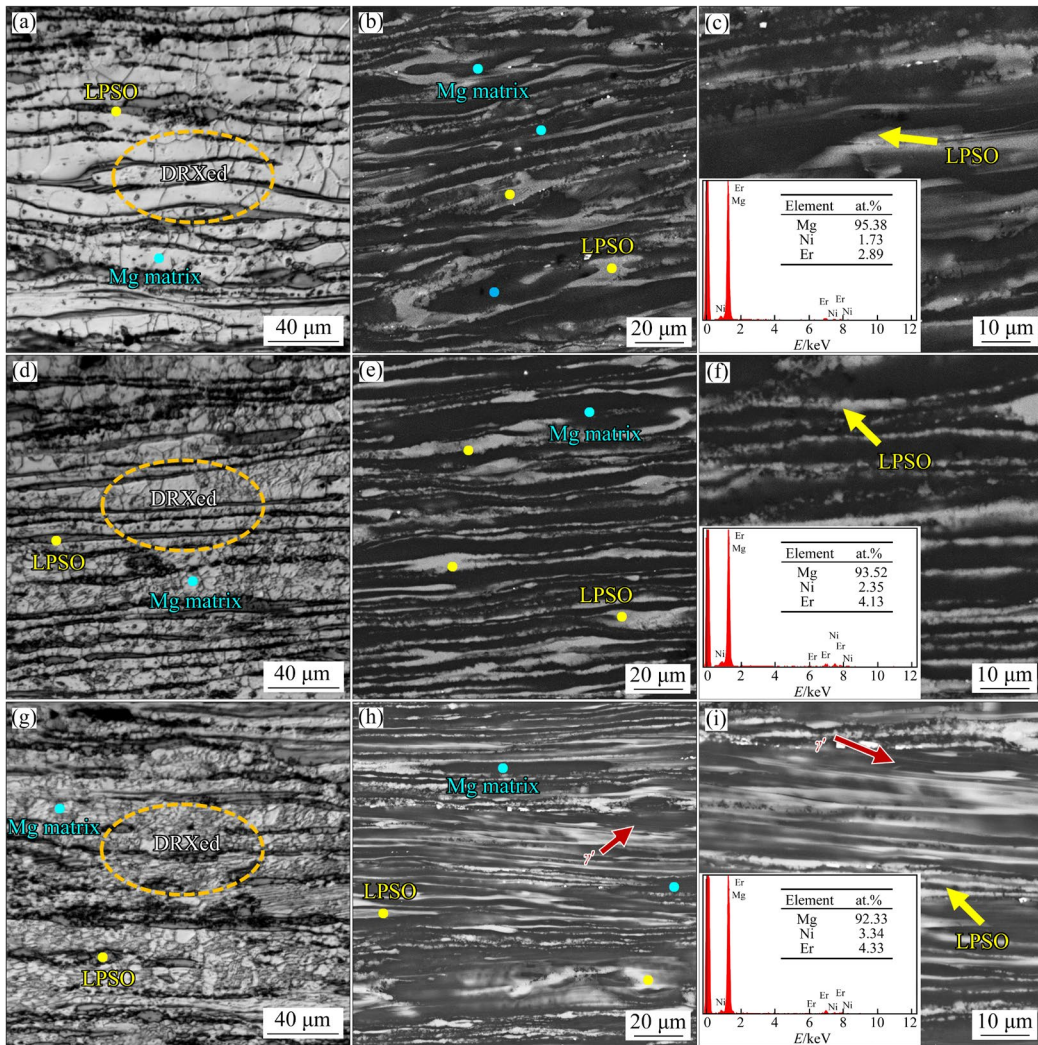
Fig. 1 OM (a, d, g) and BSE (b, e, h, c, f, i) images of as-extruded Mg−Er−Ni alloys: (a−c) EM17EN; (d−f) EM12EN; (g−i) EM9EN
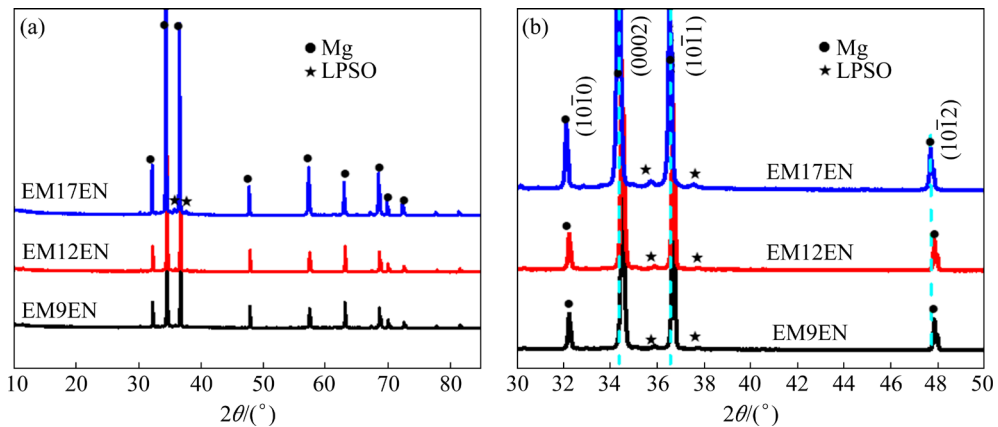

Fig. 2 XRD patterns of as-extruded Mg−xEr−1.6Ni alloys: (a) Whole XRD patterns; (b) Locally enlarged XRD patterns

The SEM morphology and corresponding EDS analyses revealed minimal changes in the LPSO phase of the alloys, while a distinct lamellar phase precipitated within the Mg matrix as the Er content decreased. Figure 3 displays TEM images of the EM9EN alloy, indicating block-like LPSO and lamellar phases. Elemental distribution maps (Figs. 3(a−c)) confirmed the presence of Mg, Er,

and Ni elements in both phases. High-resolution TEM image and selected-area electron diffraction pattern identified the block-like structure as the 18R-LPSO phase (Figs. 3(d, e)), characterized by a lattice spacing around 1.6 nm and an atomic stacking sequence of AB′C′ACACA′B′CBCBC′-A′BAB. This observation is consistent with the established research [15]. Moreover, high-resolution and selected-area electreon diffraction of the lamellar phase revealed narrower interplanar spacing and the absence of periodic extra spots. Streaks along the *c*-axis between diffraction spots (Figs. 3(f, g)) confirmed that the lamellar structure corresponds to the *γ*′ phase [16,17].

Figure 4 illustrates the inverse pole figure (IPF) and distribution of DRXed grains in the as-extruded Mg−Er−Ni alloy with varying Er contents. The black regions in the IPF maps represented the LPSO phase, while differently colored grains indicated distinct crystal orientations (Figs. 4(a−c)). Remarkably, with decreasing Er content, three alloys exhibited grain orientations along both the basal plane and non-basal plane, although the number of orientations along the basal planes increased with decreasing Er content. The

distribution of DRXed grains revealed a decrease in their fraction from 89.8% to 79.1% as Er content decreased from 17 wt.% to 9.5 wt.%, accompanied by an increase in unDRXed grains (Figs. 4(d−f)). Specifically, the EM9EN alloy displayed the lowest fraction of DRXed grains and the highest fraction of deformed grains. This trend suggested the inhibitory effect of the *γ*′ phase on dynamic recrystallization.

Figure 5 presents the (0001) pole figures, showing consistent texture characteristics across the three alloys. As Er content decreases, a slight increase in the texture intensity of the alloy becomes evident, progressing from 5.80 MRD to 7.07 MRD (Figs. 5(a, d, g)). The texture of the DRXed grains closely resembles the overall alloy texture (Figs. 5(b, e, h)), which is attributed to the high fraction of DRXed grains. The decrease in texture intensity of the DRXed grains with the decrease of Er content is particularly noteworthy, while the texture of the unDRXed grains shows the opposite trend (Figs. 5(c, f, i)). This observation aligns with the decrease in the fraction of DRXed grains and the increase in the fraction of unDRXed grains.
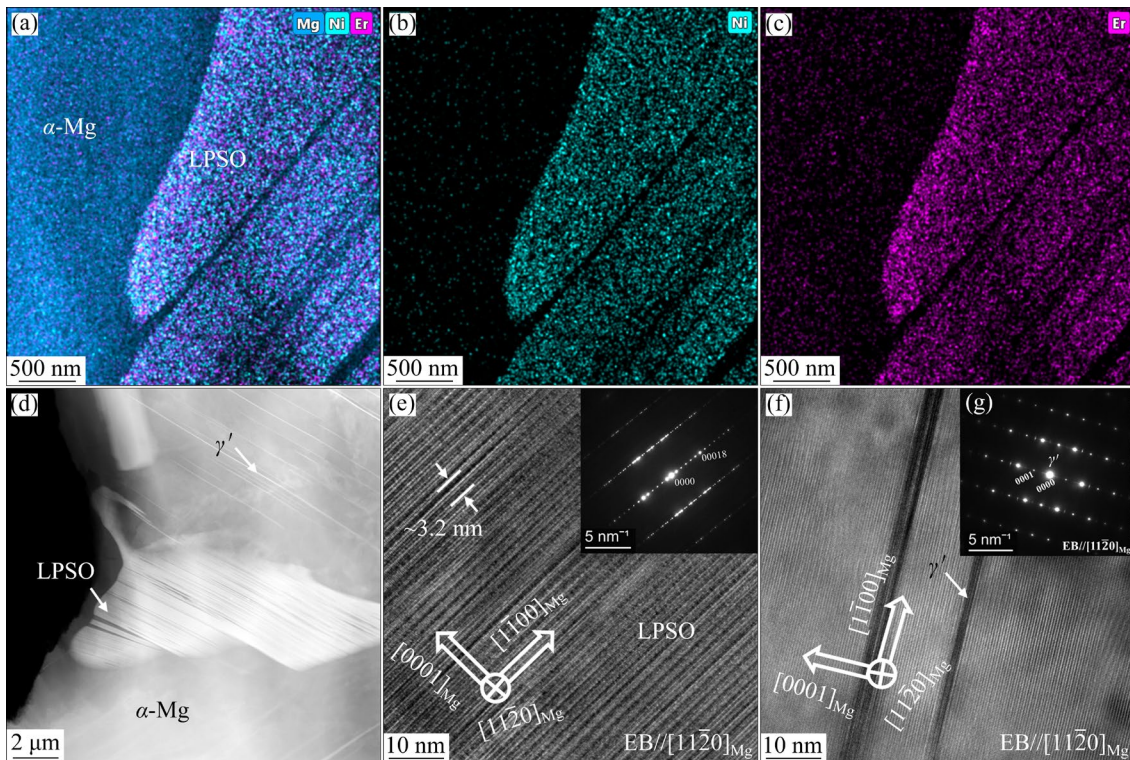

Fig. 3 EDS maps and TEM images of lamellar secondary phase and LPSO phase in EM9EN alloy: (a−c) EDS maps; (d) TEM bright field image; (e−g) HRTEM image and corresponding selected-area electron diffraction pattern, respectively
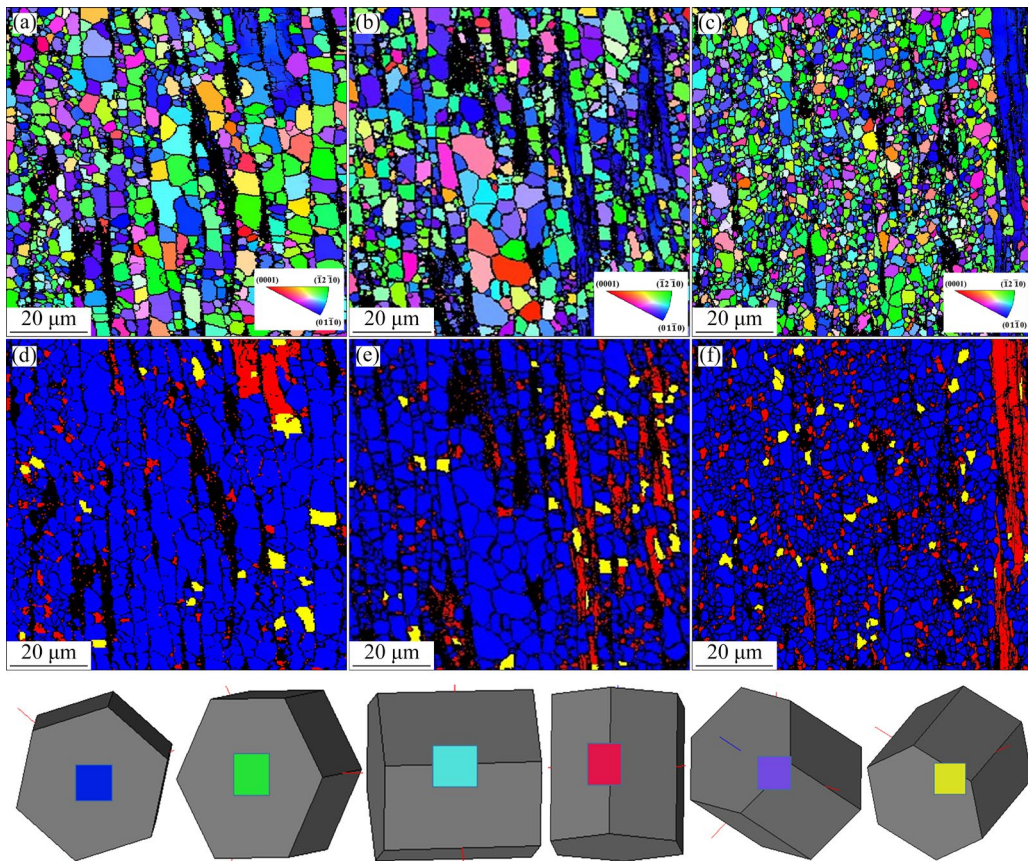
Fig. 4 IPF maps (a−c) and distribution (d−f) of DRXed grains in as-extruded Mg−*x*Er−1.6Ni alloys: (a, d) EM17EN; (b, e) EM12EN; (c, f) EM9EN
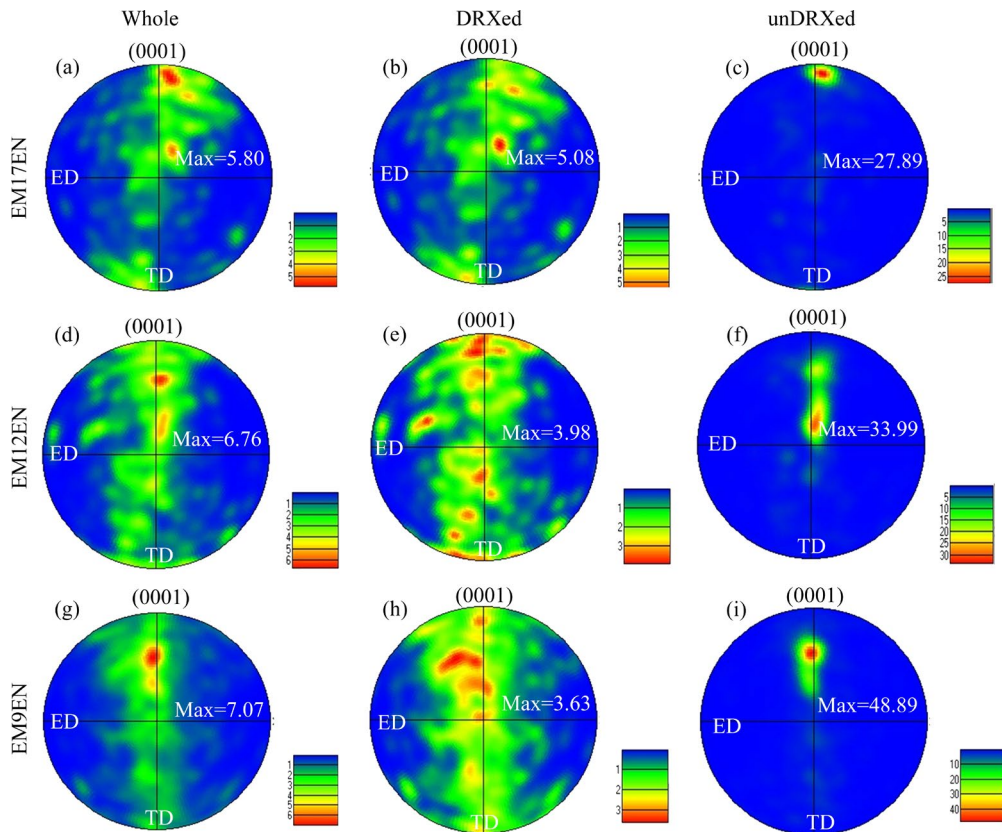

Fig. 5 (0001) pole figures of as-extruded Mg−*x*Er−1.6Ni alloys: (a−c) EM17EN; (d−f) EM12EN; (g−i) EM9EN

3.2 Mechanical properties of as-extruded Mg−xEr−1.6Ni alloy

Figure 6 presents the stress−strain curves and mechanical properties along the extrusion direction with varying compositions. The stress−strain curves of the three alloys exhibit similar behavior, which display limited work hardening after yielding (Fig. 6(a)). A slight increase in ultimate tensile strength (UTS) is observed with decreasing Er content, although this variation is not significant. Additionally, alteration in Er content minimally impacts the elongation (EL) of the alloys. However, the tensile yield strength (TYS) of the EM9EN alloy demonstrates a substantial increase by 22.3%, rising from 224 MPa for EM17EN to 274 MPa for EM9EN (Fig. 6(b)).

3.3 Corrosion behaviors of as-extruded Mg−xEr−1.6Ni alloys

3.3.1 Hydrogen evolution and mass loss

Hydrogen evolution and mass loss are critical parameters for assessing the material corrosion behavior. Hydrogen evolution quantifies the released hydrogen gas during corrosion, providing information on reaction rates and severity, while mass loss offers insights into corrosion rates and material susceptibility. Figure 7 illustrates the relationship of hydrogen evolution volume (HEV), hydrogen evolution rate (HER), and mass loss corrosion rate (MLR) in 3 wt.% KCl solution. The hydrogen evolution curve exhibits an initial rise followed by a plateau for all alloys (Fig. 7(a)). Notably, lower Er content leads to a quicker attainment of a steady-state hydrogen evolution. The analysis of the fit showed a steeper slope for the EM9EN alloy, suggesting a faster reaction rate and increased corrosion severity over the same time

duration (Fig. 7(b)). The HER analysis consistently indicates a significantly higher corrosion rate for the EM9EN alloy throughout the corrosion process compared to the EM17EN and EM12EN alloys (Fig. 7(c)). Overall, the sequence of corrosion rates follows decreasing order: EM9EN > EM12EN > EM17EN. MLR at different corrosion temperatures shows a 3−4 fold increase in the rate of MLR with decreasing Er content, which is attributed to the higher corrosion driving force at elevated temperatures. The corrosion rate of the EM12EN alloy increased by 13.1% compared to that of EM17EN, while EM9EN exhibited a substantial rise, increasing by 51.5% compared to that of EM17EN (Fig. 7(d)). This significant increase in MLR is attributed to the diminished effectiveness of the corrosion-resistant product layer due to lower Er content and the formation of the lamellar γ' phase.

3.3.2 Electrochemical properties

Figure 8 presents the EIS plot, equivalent circuit relationship, and polarization impedance. In Fig. 8(a), distinct impedance loops at different frequencies provide valuable electrochemical insights. The Nyquist plots demonstrate two capacitance loops at high and medium frequencies, accompanied by an inductance loop at low frequencies. The capacitance loops at high and medium frequencies indicate charge transfer processes associated with specific interfaces or reactions, as well as the formation of surface corrosion product film. Meanwhile, the low-frequency inductance loop corresponds to localized alloy corrosion. The diameters of the capacitance loops indicate the magnitude of charge transfer and film impedance at respective frequencies [18,19]. Larger diameters typically denote higher impedance, hindering the charge transfer processes [20]. In
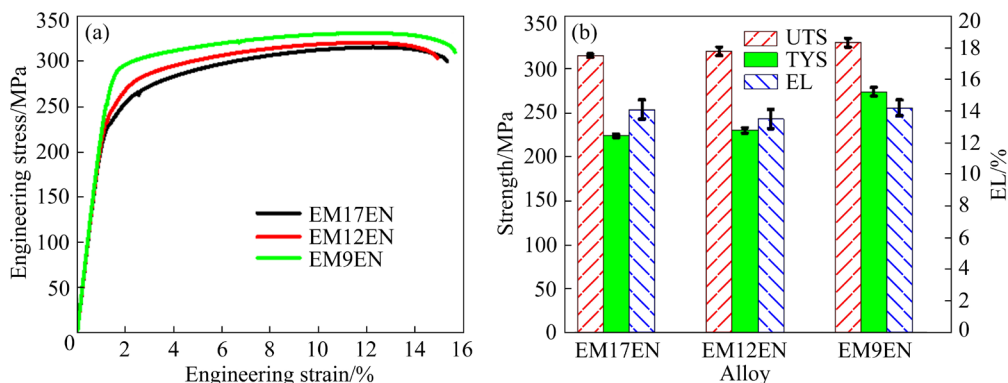

Fig. 6 Mechanical properties of as-extruded Mg−xEr−1.6Ni alloys: (a) Engineering stress−strain curves; (b) Tensile properties
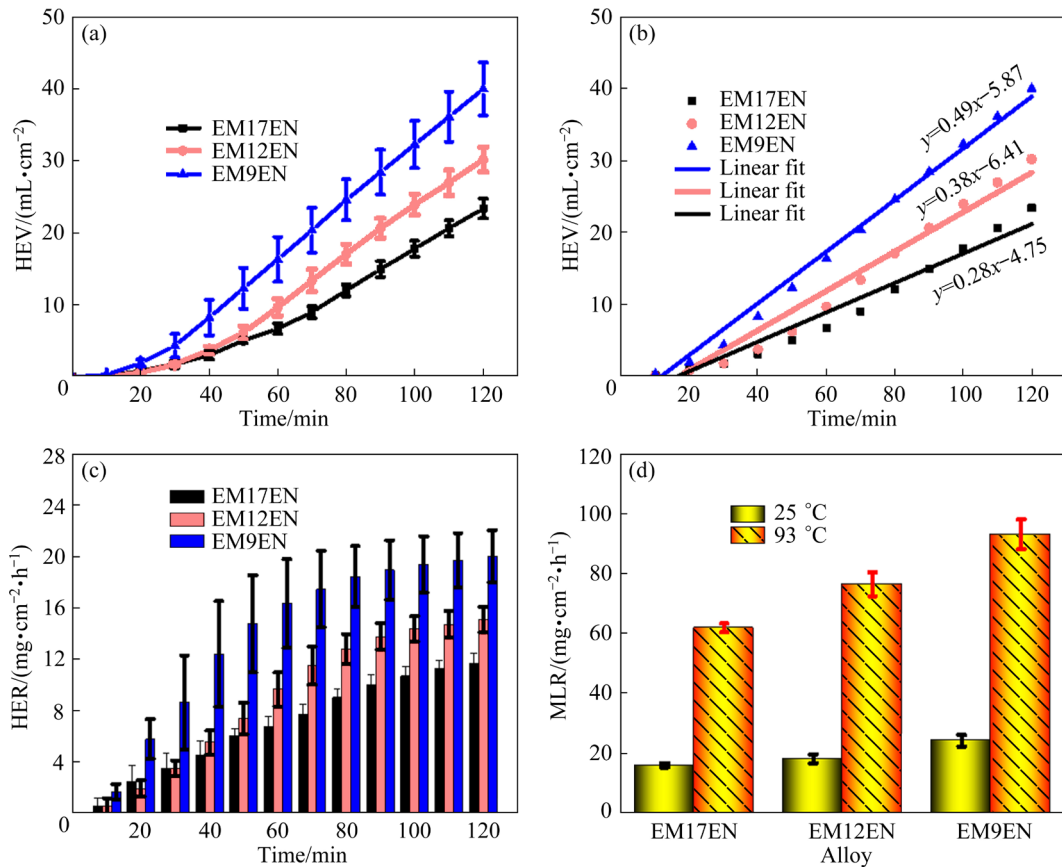
Fig. 7 Corrosion evaluation of as-extruded Mg−xEr−1.6Ni alloys: (a, b) Hydrogen evolution volume with immersion time; (c) Hydrogen evolution rate with immersion time; (d) Mass loss rate at different immersion temperatures
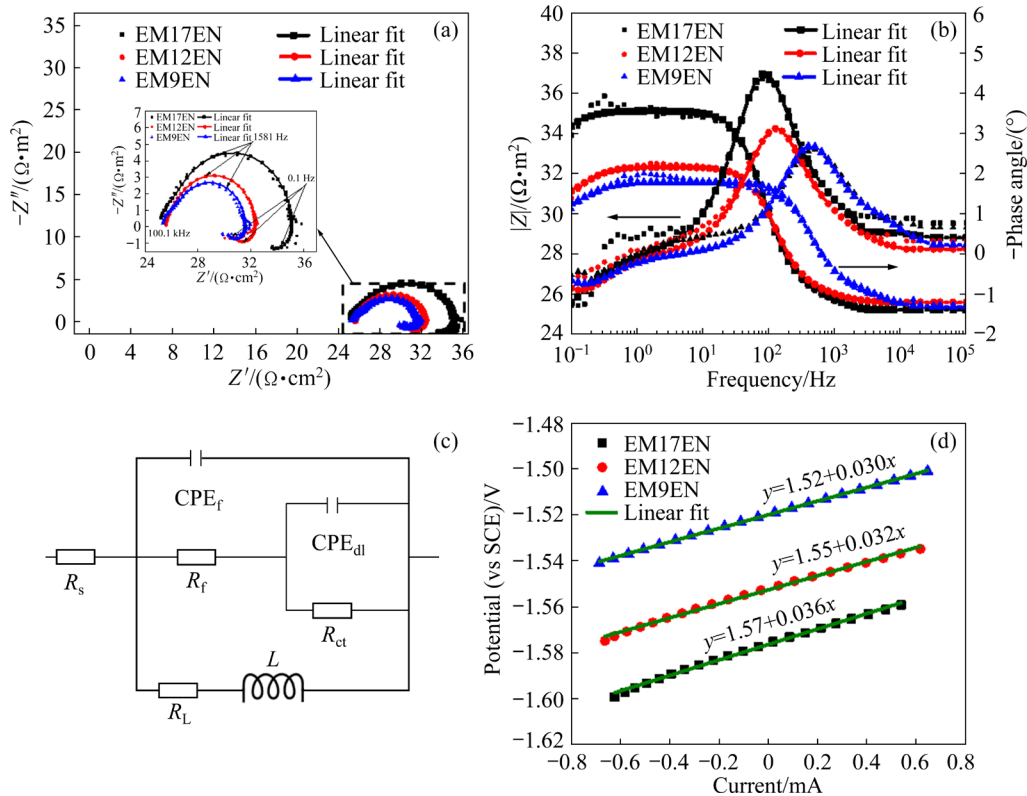

Fig. 8 Electrochemical characterization results of as-extruded Mg−xEr−1.6Ni alloys immersed in 3 wt.% KCl solution at room temperature: (a) Nyquist plots; (b) Bode plots; (c) Equivalent circuit plot; (d) Polarization curves

comparison to other alloys, smaller diameters in the Nyquist plots for the EM9EN alloy suggest lower impedance, indicating more facile and active charge transfer processes and corrosion reactions. Therefore, EM9EN alloy exhibits higher corrosion susceptibility and greater degradation rates.

The Bode plots in Fig. 8(b) provide insights into angle and impedance magnitude variations ($|Z|$) with frequency. The phase angle−frequency plots indicate the presence of two peaks, signifying two capacitive loops at high and medium frequencies across all the as-extruded Mg−xEr−1.6Ni alloys, which aligns with the results of the Nyquist plot. Furthermore, the $|Z|$ versus frequency plots reveal an increase in impedance values from high to medium frequencies, followed by a decrease in the low-frequency range. Notably, the low-frequency $|Z|$ region serves as an indicator for assessing corrosion rates of Mg alloy, where lower $|Z|$ values correspond to higher corrosion rates [21]. Hence, the lower $|Z|$ value observed in the low-frequency region suggests a higher corrosion tendency and increased susceptibility to corrosion reactions in the EM9EN alloy.

The equivalent circuit diagram is shown in Fig. 8(c) and the fitting parameters are presented in Table 1. In this circuit, R_s represents solution resistance, R_{ct} and CPE_{dl} correspond to charge transfer resistance and double-electric layer capacitance, respectively. Meanwhile, R_f and CPE_f represent film resistance and capacitor in the midium frequency range. Furthermore, L and R_L represent the inductance and inductive resistance, respectively indicating the breakdown of the protective film influenced by the absorbed Mg^{2+} reaction with H_2O. These components collectively indicate the occurrence of localized corrosion, characterized by the degradation of the protective film and the initiation of corrosive reactions. Moreover, the constant phase element (CPE) serves as an alternative to the ideal capacitor, accommodating surface heterogeneity on the alloy [22]. The

parameters n_1 and n_2 represent dispersion coefficients, addressing the non-ideal behavior of the system. These equivalent circuit parameters offer insights into electrochemical impedance (R_p), calculated as $R_p = R_f + R_{ct} \cdot R_L / (R_{ct} + R_L)$. Lower values of R_p, R_{ct}, and R_f observed in the EM9EN alloy indicate rapid degradation and higher film rupture properties. Similar trends are evident in the electrochemical transient polarization impedance analysis depicted in Fig. 8(d). A gradual decline in the slope of the fitted polarization curve is observed with decreasing Er content, notably with the EM9EN alloy displaying the lowest polarization impedance. This observation aligns with the EIS results, indicating that alloys become more susceptible to corrosion as the Er content decreases during electrochemical corrosion.

The polarization curves and fitted parameters in Fig. 9 provide valuable insights into the electrochemical behavior of the as-extruded Mg−xEr−1.6Ni alloys with varying Er contents. In Fig. 9(a), similar patterns are observed in the polarization curves for the three alloys, consisting of an anodic branch representing Mg alloy dissolution ($Mg^{2+} + 2H_2O = Mg(OH)_2 + 2H^+$) and a cathodic branch associated with the hydrogen evolution reaction ($2H_2O + 2e = 2OH^- + 2H_2\uparrow$). Within the cathodic branch, the corrosion current density (J_{corr}) follows a increasing trend of EM17EN < EM12EN < EM9EN, suggesting that the EM9EN alloy displays the highest corrosion rate. Quantitative Tafel extrapolation calculations (Fig. 9(b)), performed in the range of 70−200 mV (vs SCE), reveal relatively minor fluctuations in corrosion potential, consistently maintained at −1.55 V (vs SCE). However, a significant change was observed in J_{corr}. As Er content decreases, J_{corr} rises significantly by orders of magnitude, indicating a substantially higher corrosion driving force in the EM9EN alloy. These findings consistently align with the results obtained from the EIS analysis.

Table 1 Fitting results of EIS spectra

Alloy	R_s/ ($\Omega \cdot cm^2$)	CPE_{dl}/ ($\mu\Omega^{-1} \cdot cm^{-2} \cdot s^n$)	n_1	R_{ct}/ ($\Omega \cdot cm^2$)	CPE_f/ ($\mu\Omega^{-1} \cdot cm^{-2} \cdot s^n$)	n_2	R_f/ ($\Omega \cdot cm^2$)	L/ ($H \cdot cm^{-2}$)	R_L/ ($\Omega \cdot cm^2$)	R_p/ ($\Omega \cdot cm^2$)
EM17EN	25.13	22.25	0.93	3.317	65.78	0.83	6.69	41.73	9.95	4.99
EM12EN	25.58	87.11	0.92	2.56	164.1	0.84	4.17	25.58	7.44	3.53
EM9EN	25.35	209.41	0.95	2.01	587.7	0.85	3.29	11.44	5.45	2.68

3.3.3 Corrosion morphologies

Figure 10 shows the corrosion morphologies of Mg−xEr−1.6Ni alloys at room temperature with various Er contents after the removal of corrosion products following a fixed corrosion duration. These illustrations exhibit distinct variations in morphology with decreasing Er content, indicating an escalation in corrosion severity. The alloys containing higher Er contents show partially uncorroded zones after the same corrosion duration, while alloys with lower Er contents exhibit intensified corrosion regions (Figs. 10(a, d, g)). Upon magnifying mild corrosion regions, it becomes evident that predominant corrosion occurs
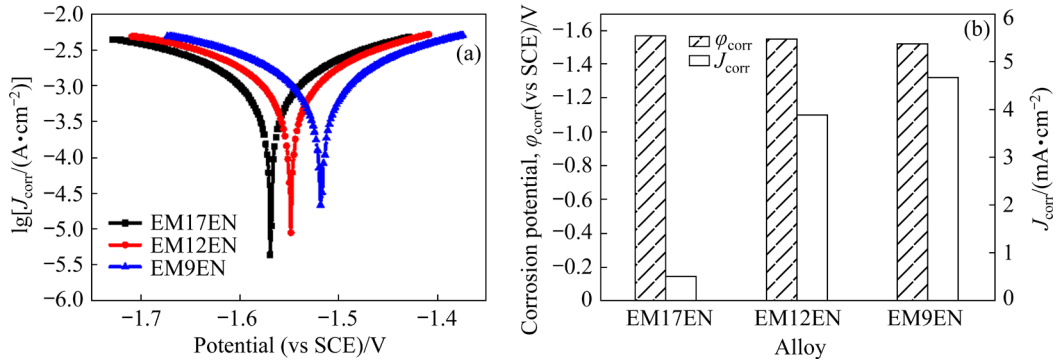
Fig. 9 Electrochemical evaluation of as-extruded Mg−xEr−1.6Ni alloys in 3 wt.% KCl solution at room temperature: (a) Polarization curves; (b) Electrochemical parameters
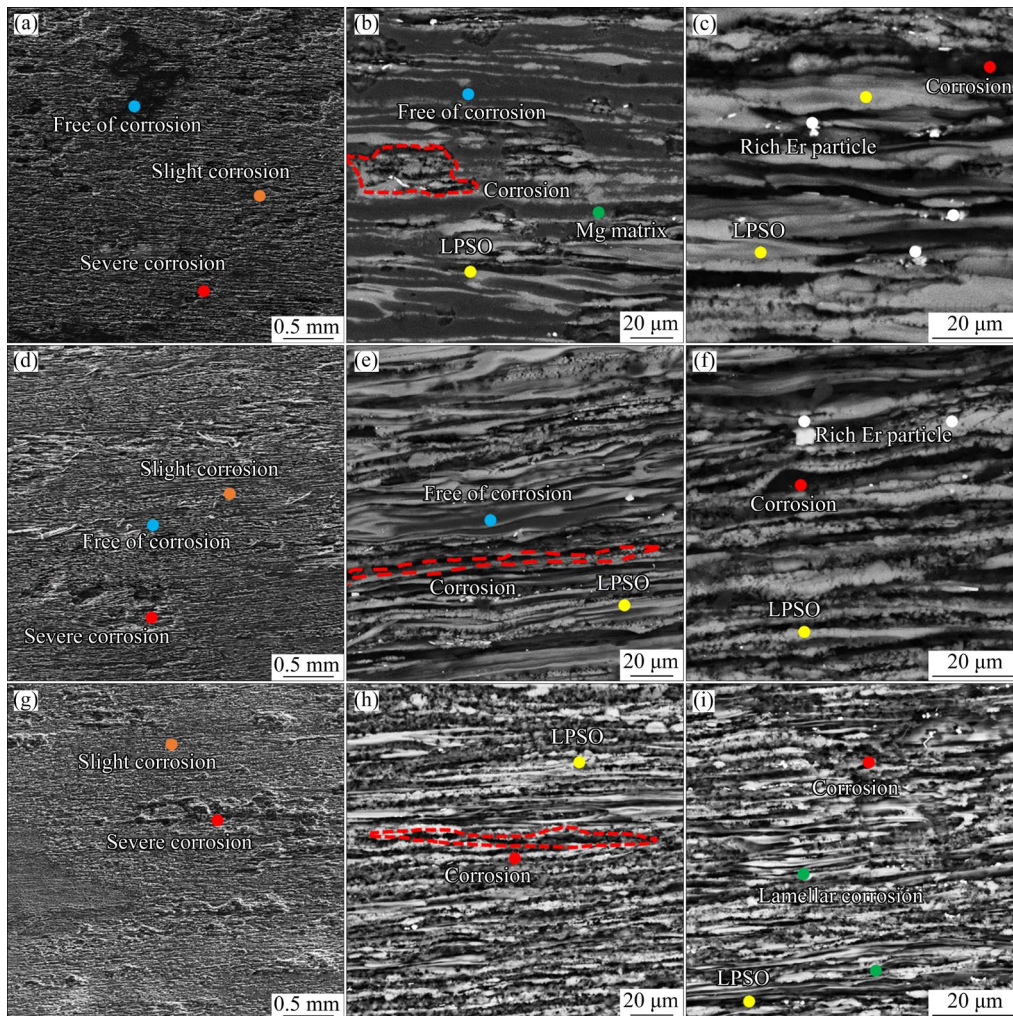
Fig. 10 SEM images of surface of as-extruded Mg−Er−Ni alloys immersed in 3 wt.% KCl solution for 5 min at room temperature after removal of corrosion products: (a−c) EM17EN; (d−f) EM12EN; (g−i) EM9EN

at the LPSO phase−Mg matrix interface, presenting as grooved patterns along the extrusion direction (Figs. 10(b, e, h)). Additionally, a shift from pitting corrosion to elongated features is observed as Er content decreases, signifying accelerated corrosion expansion in the EM9EN alloy compared to alloys with higher Er contents. In severe corrosion regions, significant corrosion of the Mg matrix between LPSO phases is evident (Figs. 10(c, f, i)). Here, the LPSO phase acts as the cathode, preferentially corroding the Mg matrix. Moreover, the presence of larger corrosion pits along the extrusion direction and distinctive lamellar corrosion structures aligns with decreased Er content, suggesting intensified corrosion effects. This observation suggests that, in addition to galvanic corrosion of the LPSO phase with the Mg matrix, galvanic corrosion of the γ' phase with the Mg matrix is also involved.

3.3.4 Corrosion films

XPS analysis was employed to investigate the chemical composition and alterations in corrosion product layers formed in 3 wt.% KCl solution for Mg−xEr−Ni alloys with varying Er contents. The peak fitting results of Mg 1s, O 1s, and Er 4d are presented in Fig. 11. The high-resolution spectra of Mg 1s (Figs. 11(a, b, c)) and O 1s (Figs. 11(d, e, f)) demonstrate that the predominant constituents of the corrosion products in the alloys are MgO and Mg(OH)$_2$, which is consistent with previous studies [23,24]. It is noteworthy that the decrease in Er content leads to more pronounced characteristic peaks of Mg(OH)$_2$, indicating intensified corrosion in alloys with low Er contents. Moreover, corrosion product of Er$_2$O$_3$ was observed in the EM17EN and EM12EN alloys (Figs. 11(g, h)), while it was not present in the EM9EN alloy (Fig. 11(i)). The lack of
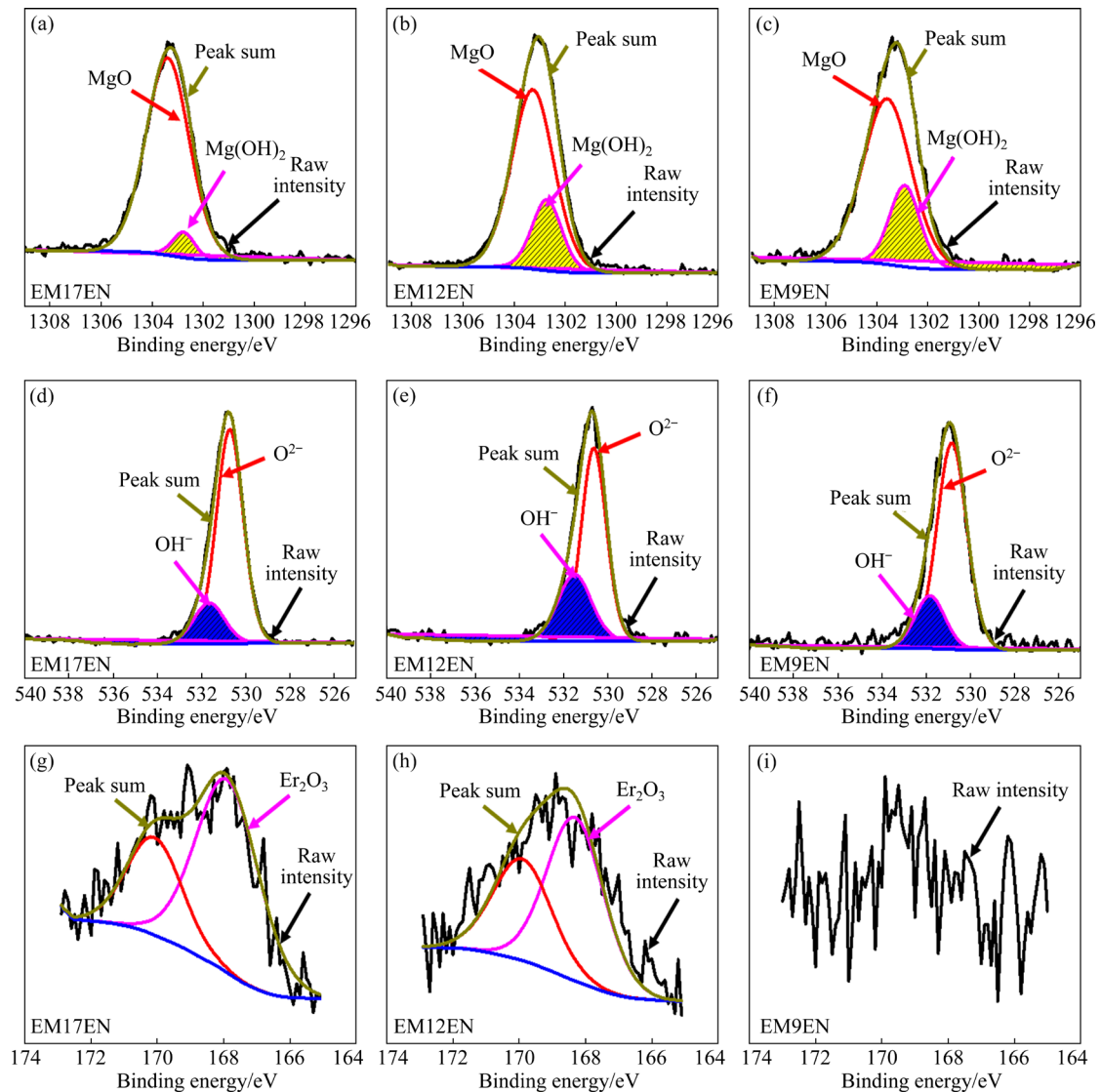

Fig. 11 XPS peak fitting results of corrosion products in as-extruded Mg−xEr−1.6Ni alloys immersed in 3 wt.% KCl solution for 10 min: (a−c) Mg 1s; (d−f) O 1s; (g−i) Er 4d

the corrosion-resistant film in the EM9EN alloy could have a significant impact on its corrosion properties.

XRD analysis was conducted on the corroded surface after a 10 min immersion, and the results are shown in Fig. 12. The analysis revealed that the corroded surface primarily consisted of the LPSO phase (36-1273#), Mg matrix (35-0821#), and $Mg(OH)_2$ (44-1482#), indicating the presence of multiple corrosion products. Notably, the thin corrosion product film permitted the identification of both the LPSO phase and the Mg substrate due to the comparatively short immersion duration. Therefore, $Mg(OH)_2$ is identified as the predominant corrosion product, and the intensity of its characteristic diffraction peaks increases with decreasing Er content. This implies a higher degree of crystallinity in the corrosion products on the alloy surface, providing further evidence of the severer corrosion in the EM9EN alloy.
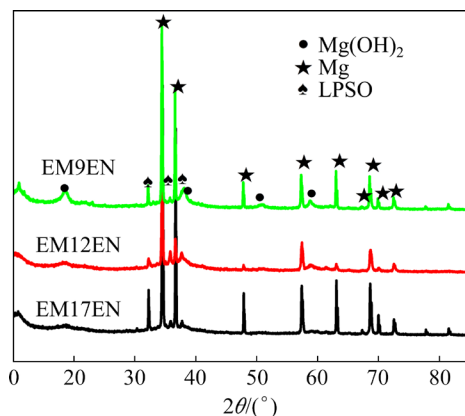

Fig. 12 XRD patterns of corrosion products on surface of as-extruded Mg−xEr−1.6Ni alloys after immersion in 3 wt.% KCl solution for 10 min

4 Discussion

4.1 Mechanism of high corrosion rate of as-extruded Mg−xEr−1.6Ni alloy with low Er contents

The mass loss rates (Fig. 7) indicate that the corrosion rate of the EM12EN alloy increased by 13.1% compared to that of the EM17EN alloy, while the corrosion rate of the EM9EN alloy significantly rose by 33.9% compared to that of the EM12EN alloy. Moreover, a streamlined distribution along the extrusion direction is maintained in the LPSO phase, with minimal variation observed as Er content decreases. However, the lamellar γ' phases form at low Er

contents. From the grain size (GS) distribution shown in Figs. 13(a, c, e), a significant refinement of GS is observed as Er content decreases. The average GS (AGS) of the EM9EN alloy experiences a significant decrease from 2.57 to 1.37 μm, whereas the changes in AGS for the EM17EN and EM12EN alloys are minimal. Furthermore, the kernel average misorientation (KAM) diagrams in Figs. 13(b, d, f) indicate an increase in the KAM value as Er content decreases, suggesting a higher density of dislocations on the EM9EN alloy. Therefore, dislocations likely play a pivotal role in driving the increased corrosion rate of the EM9EN alloy. Moreover, the three alloys exhibit a basal fiber texture with consistent texture intensity (Fig. 5), suggesting that the effect of texture on the enhancement of corrosion rate can be negligible. Nevertheless, the alloy orientations in this study demonstrate complexity, necessitating further investigation to elucidate their influence on corrosion behavior. It is worth noting that as the Er content decreases, the corrosion-resistant Er_2O_3 film cannot be formed, thus weakening its corrosion inhibition effect. Therefore, to elucidate the underlying mechanism of the substantial increase in the corrosion rate of the EM9EN alloy, it is essential to discuss the effects of GS, dislocation density, γ' phase, grain orientation, and corrosion product films on corrosion performance.

The impact of GS on the corrosion rate has long been a subject of controversy among researchers. Some believe that reducing GS promotes the formation of protective films along grain boundaries, thus hindering corrosion propagation [25]. In contrast, some propose that a decreased GS introduces grain boundary defects, providing sites for corrosion to occur and thereby accelerating the overall corrosion process [26]. In the investigation of soluble Mg-based alloys, NIU et al [27] observed that the grain refinement significantly accelerated the corrosion rate of the as-extruded Mg−Zn−Ni alloys. Similarly, ZHONG et al [28], also observed accelerated degradation with a finer grain size in Mg alloys, especially with Ni addition, consistent with our previous studies [11,29]. Consequently, the EM9EN alloy, characterized by the grain refinement, exhibits significant contrast to minimal GS changes in EM17EN and EM12EN alloys. This indicates that the grain refinement plays a crucial role in influencing
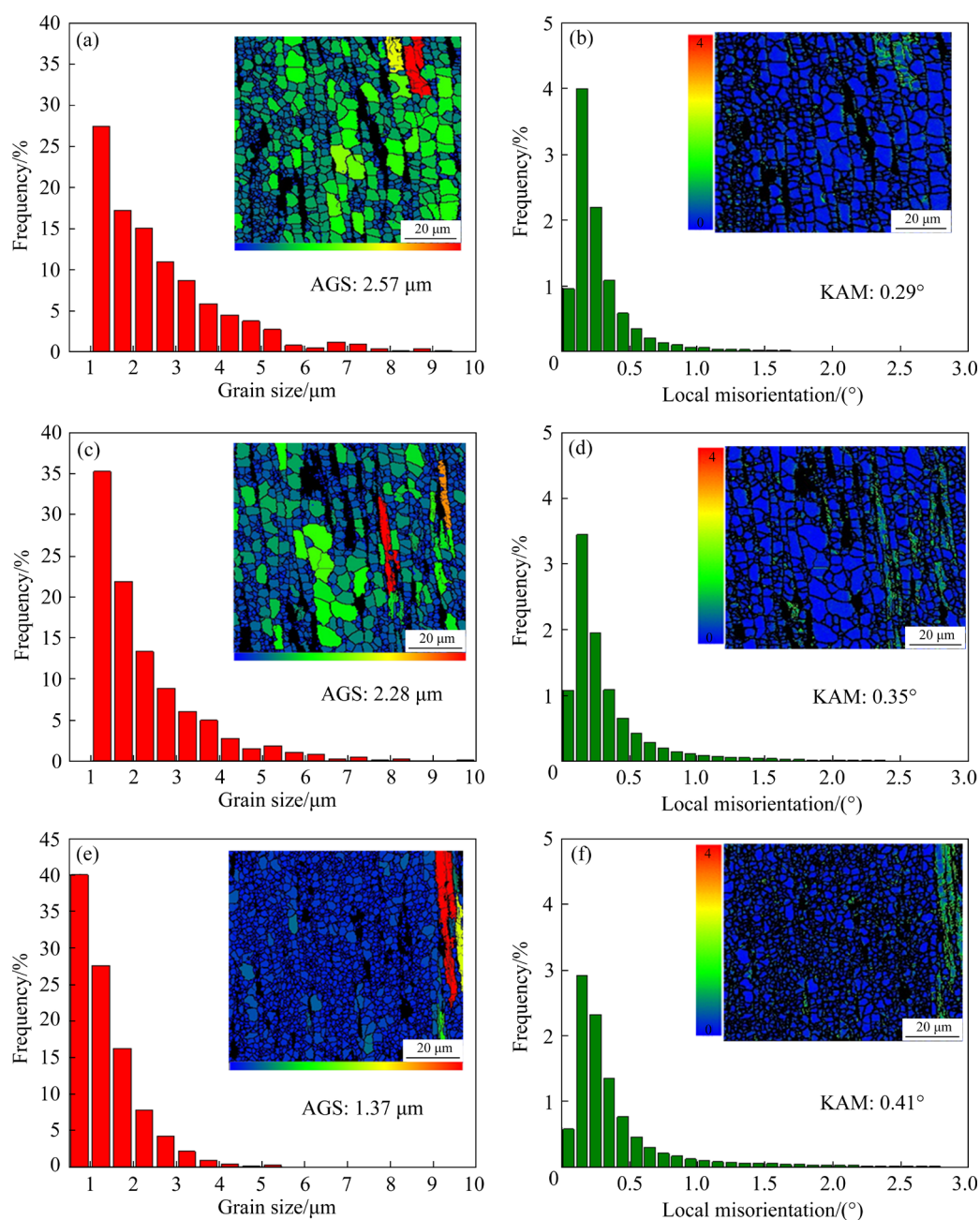
Fig. 13 GS distribution (a, c, e) and KAM maps (b, d, f) of as-extruded Mg−xEr−1.6Ni alloys: (a, b) EM17EN; (c, d) EM12EN; (e, f) EM9EN

the corrosion behavior of the Mg−xEr−1.6Ni alloy, particularly enhancing the degradation rate of the EM9EN alloy.

With decreasing Er content, there is a corresponding increase in the corrosion rate, accompanied by a rise in dislocation density. Notably, the increments in dislocation density are similar between the EM12EN and EM17EN alloys, as well as between the EM9EN and EM12EN alloys. This implies that if dislocations serve as the primary factor driving corrosion, the increase in corrosion rate will be comparable for the EM9EN

alloy. Hence, the influence of dislocations on the enhancement of corrosion rate in the EM9EN alloy is not predominant. This observation aligns with the research conducted by MA et al [29] on high-strength Mg−Gd−Ni alloys, who reported a minimal impact of dislocations on the corrosion behavior.

The impact of the γ' phase on the corrosion behavior of alloys has received relatively limited attention. ZHANG et al [30] investigated the corrosion morphologies of the Mg−Gd−Y−Zr alloy containing the γ' phase. Their observations revealed

preferential corrosion of the Mg matrix in proximity to the γ' phase, while the elements rich in Gd, Zn, and Zr within the γ' phase remained unaffected by corrosion. This suggests the γ' phase acted as a cathode, accelerating the corrosion of alloy. DAI et al [31] also found that the corrosion rate of the alloy was similarly enhanced by introducing a higher density of γ' phase in Mg−Er−Ni alloy. They reported a comparable augmentation in the corrosion rate of the alloy when introducing a higher density of the γ' phase in Mg−Er−Ni alloy. In the Mg−xEr−1.6Ni alloy, a decrease in Er content results in the precipitation of internal lamellar γ' phases. These phases could contribute to the creation of new corrosion sites, ultimately accelerating the overall corrosion rate of the alloy.

The grain orientations in the three alloys, as depicted in Fig. 4, exhibit a relatively complex pattern, mainly comprising basal crystal orientations (blue and green) and non-basal crystal orientations (other colors). A stronger basal texture in the EM9EN alloy is evident with a higher number of grains exhibiting basal crystal orientations, which are generally considered less susceptible to alloy corrosion [32]. Therefore, in this study, the impact of grain orientations on the enhanced corrosion rate in these alloys appears to be minimal.

According to the corrosion morphology, surface morphology of corrosion products, and compositional analysis shown in Figs. 10−12, it can be concluded that corrosion is intensified with a decrease in Er content. Predominantly, corrosion occurs between the LPSO phase and Mg matrix, with the corrosion products transitioning from $Mg(OH)_2$ and Er_2O_3 to $Mg(OH)_2$, as depicted in Fig. 14. In the initial stage of corrosion in all alloys, galvanic corrosion dominates (Figs. 14(a, c, e)), with a preference for corroding the Mg matrix due to the higher potential of the LPSO phase [33]. With prolonged corrosion, the EM17EN and EM12EN alloys form a composite $Er_2O_3/Mg(OH)_2$ layer, effectively hindering further corrosion [34]. Moreover, the EM12EN alloy, characterized by lower Er content, develops less dense corrosion products, which contributes to localized corrosion and a slightly higher corrosion rate (Figs. 14(c, d)). In contrast, the EM9EN alloy demonstrates a less compact $Mg(OH)_2$ corrosion product layer, resulting in minimal inhibition to the corrosion

reaction (Fig. 14(f)). Furthermore, the existence of the lamellar γ' phase within the EM9EN alloy not only enhances intergranular corrosion but also promotes galvanic corrosion within the grains, leading to a substantial acceleration of the corrosion process. Consequently, the substantial increase in degradation rate in the EM9EN alloy is primarily attributed to the galvanic corrosion of the γ' phase and Mg matrix, intergranular corrosion, and the disruption of corrosion-resistant Er_2O_3 film.

4.2 Mechanism of high TYS of as-extruded Mg−xEr−1.6Ni alloy with low Er contents

As the Er content decreases, there is a significant increase in the TYS, particularly in the EM9EN alloy, showing a 22.3% enhancement compared to that of the EM17EN alloy, while the elongation remains relatively unchanged at around 14% (Fig. 6). The Schmid factor (SF) can be used to describe the probability of slip activation in a specific direction, in which the higher the value of the basal SF, the greater the possibility of slip activation [29]. Figure 15 illustrates that the SF values for the basal and prismatic planes are comparable, with the SF values for the prismatic plane being significantly higher than those for the basal plane. This suggests that the slip along the non-basal planes is more favorable. In addition, considering that all alloys display a basal texture, the alloys with lower SF values for the basal plane have greater difficulty in slip activation, ultimately contributing to an enhanced TYS [35]. Therefore, the impact of texture strengthening on the enhancement of TYS is similar among all alloys. Moreover, as Er content decreases, the AGS decreases from 2.57 to 1.37 μm (Fig. 13), indicating a potentially substantial impact of grain boundary strengthening on the improvement of the TYS [33].

In Mg−xEr−1.6Ni alloy, the primary secondary phases were LPSO and γ' phases due to negligible solid solubility of Ni (Fig. 3). These phases consumed a comparable amount of Er and Ni, while the remaining Er was solid-solution strengthened within the Mg matrix [36]. Moreover, the presence of γ' phase, particularly in the EM9EN alloy, played a significant role in enhancing the TYS [11]. Furthermore, the dislocations generated during the extrusion process indicate that, with decreasing Er content, the KAM value increases, reflecting higher dislocation density and enhanced strengthening
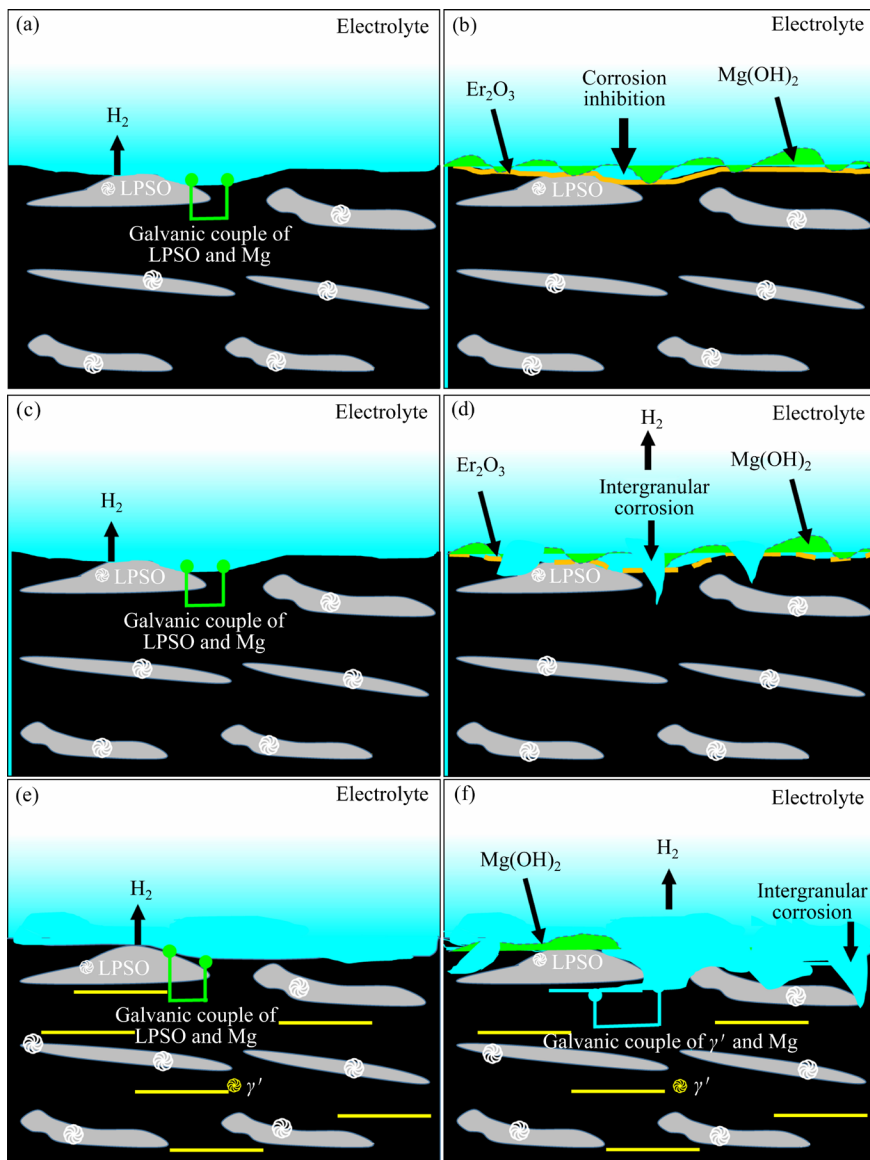
Fig. 14 Corrosion mechanism illustration of as-extruded Mg−*x*Er−1.6Ni alloys: (a, b) EM17EN; (c, d) EM12EN; (e, f) EM9EN

effects. Overall, the enhancement of TYS in Mg−*x*Er−1.6Ni alloys was attributed to the combined effects of solid-solution strengthening ($\Delta\sigma_{ss}$), dislocation strengthening ($\Delta\sigma_{ds}$), grain refinement strengthening ($\Delta\sigma_{gs}$), and secondary phase strengthening ($\Delta\sigma_{sd}$).

The influence of $\Delta\sigma_{ss}$ is dependent on the amount of Er atoms in the Mg matrix. Previous studies [33,37] indicated a direct relationship between $\Delta\sigma_{ss}$ and the element content, where Ni content is 0.84 at.%, and the Er contents, from high to low, are 2.92 at.%, 1.96 at.%, and 1.52 at.%. Consequently, the contribution of $\Delta\sigma_{ss}$ to the TYS of the EM17EN, EM12EN, and EM9EN alloys is 97.5, 78.6, and 62.4 MPa, respectively. Among

them, the EM17EN alloy showed the highest $\Delta\sigma_{ss}$ effect, suggesting that $\Delta\sigma_{ss}$ is not the main factor for the significant increase in TYS in the EM9EN alloy.

Another important factor is dislocation [38], which can be assessed through the KAM values. The KAM values for the EM17EN, EM12EN, and EM9EN alloys are 0.29°, 0.35°, and 0.41°, respectively. The difference in KAM values between the EM17EN and EM12EN alloys is 0.06°, and the KAM difference between the EM12EN and EM9EN alloys is also 0.06°, suggesting a comparable effect of $\Delta\sigma_{ds}$ on the enhancement of TYS. Therefore, the substantial increase in TYS in the EM9EN alloy implies that the impact of $\Delta\sigma_{ds}$ on the TYS is relatively minor. The contribution of
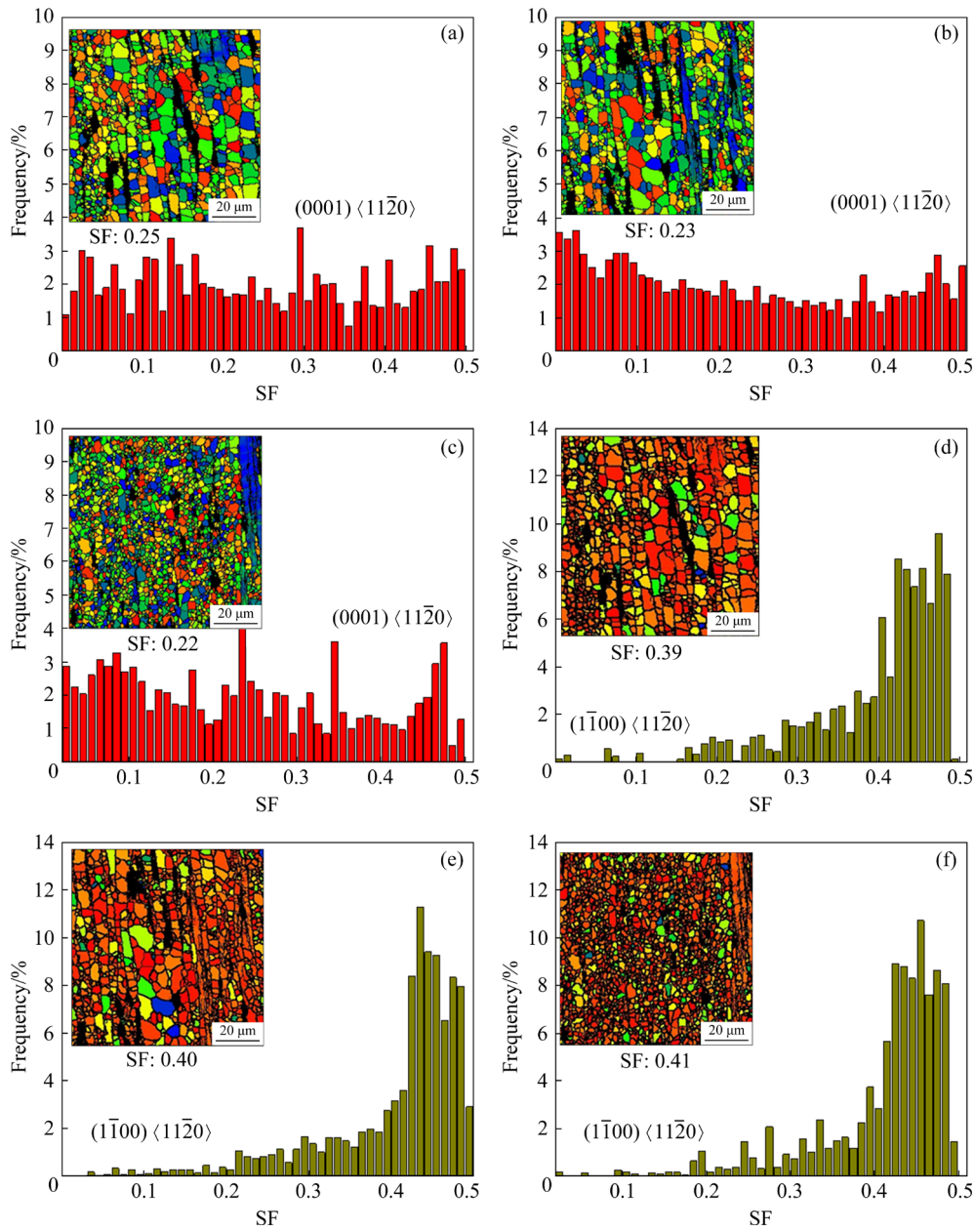
Fig. 15 SF distribution for basal slip (a−c) and prismatic slip (d−f) of as-extruded Mg−xEr−1.6Ni alloys: (a, d) EM17EN; (b, e) EM12EN; (c, f) EM9EN

dislocations to the TYS can be calculated from the following equation:

$$\Delta\sigma_{ds} = V_{unDRXed} M\alpha Gb\sqrt{\rho_{unDRXed}} \qquad (1)$$

where $V_{unDRXed}$ and $\rho_{unDRXed}$ are the volume fraction of deformed grains and dislocation density, respectively, M is the Taylor factor (3.06), α is a constant of 0.2, G is the shear modulus (1.66×10^4 MPa), and b is the amplitude of Burgers vector (3.21×10^{-10} m). While $\rho_{unDRXed}$ was obtained from Ref. [39], the contribution of $\Delta\sigma_{ds}$ to the TYS of EM17EN, EM12EN, and EM9EN alloys is 3.3, 5.8, and 6.8 MPa, respectively.

In addition, the strengthening of fine grains is considered to be an effective way to enhance the mechanical properties of alloys. In Mg−xEr−Ni alloys, the GS is gradually refined as the Er content decreases, albeit with varying degrees. Specifically, the EM12EN alloy shows a refinement of 0.29 μm compared to the EM17EN alloy, and the EM9EN alloy exhibits a refinement of 0.91 μm compared to the EM12EN alloy. Meanwhile, the fraction of DRXed grains remains relatively consistent among the alloys. Subsequently, the contribution of $\Delta\sigma_{gs}$ to the TYS of EM17EN, EM12EN, and EM9EN alloys is 113.3, 119.6, and 151.1 MPa, respectively.

Thus, $\Delta\sigma_{gs}$ induced by the fine GS emerges as a crucial factor in the notable increase in TYS of the EM9EN alloy [38].

Distinctively, except for the bulk LPSO phase, the lamellar γ' phase precipitates within the Mg matrix for the EM9EN alloy with low Er content. Moreover, mechanical properties show that the TYS of the EM17EN, EM12EN, and EM9EN alloys is 224, 226, and 274 MPa, respectively. Consequently, the $\Delta\sigma_{sd}$ can be approximately calculated using the equation $\Delta\sigma_{sd}=\Delta\sigma_{0.2}-\Delta\sigma_{ss}-\Delta\sigma_{ds}-\Delta\sigma_{gs}$, with contribution to TYS of 9.9, 22.0, and 53.7 MPa, respectively. Thus, the larger difference of $\Delta\sigma_{sd}$ among alloys suggests that a significant role of the lamellar γ' phase plays in enhancing the TYS of EM9EN alloys.

Therefore, the enhancement of TYS in the EM9EN alloy can be attributed to the combined effects of $\Delta\sigma_{gs}$ and $\Delta\sigma_{sd}$ resulting from grain refinement and the precipitation of lamellar γ' phases. While $\Delta\sigma_{ss}$ and $\Delta\sigma_{ds}$, although present to some extent, do not significantly contribute to the enhancement of TYS in the EM9EN alloy with low Er content.

5 Conclusions

(1) The decrease of Er content promotes a transition in the phase component of Mg alloy from the predominant LPSO phase to a coexistence of LPSO phase and γ' phase without significantly altering the overall content and distribution of the secondary phase.

(2) The γ' phase, which is promoted to be formed at low Er content, has a dual effect. On the one hand, the presence of γ' phase inhibits dynamic recrystallization and strengthens grain boundaries through grain size refinement. On the other hand, it also plays a role in secondary phase strengthening, resulting in a synergistic increase of TYS by 22.3% for the EM9EN alloy.

(3) Compared with the EM17EN alloy, the EM9EN alloy experiences stronger intergranular corrosion caused by grain refinement, as well as more corrosion sites created by the introduction of the γ' phase and the disruption of the corrosion-resistant Er_2O_3 film, which contributes to the increase in the corrosion rate of the EM9EN alloy by 51.5%.

(4) The synergistic enhancement in both corrosion and mechanical properties of the EME9N alloy has been achieved by reducing the Er content, which introduces the γ' phase into the alloy and refines the grains. The concept for the mix design of the Er-containing Mg alloy proposed in this study lays the foundation for the design of high-strength and high-degradation alloys.

CRediT authorship contribution statement

Chao-neng DAI: Conceptualization, Methodology, Investigation, Writing – Original draft; **San-lue PEI:** Data curation, Writing – Review & editing; **Ye WANG:** Data curation, Validation, Writing – Review & editing; **Zi-hong WANG:** Writing – Review & editing; **Jin-xing WANG:** Methodology, Writing – Review & editing; **Yan-long MA:** Writing − Review & editing; **Jing-feng WANG:** Conceptualization, Supervision, Visualization.

Declaration of competing interest

The authors declare that they have no known competing financial interests or personal relationships that could have appeared to influence the work reported in this paper.

Data availability

The raw/processed data required to reproduce these findings cannot be shared at this time as the data also forms part of an ongoing study.

References

[1] MA Hui-yun, YU Cheng-gang, SHUAI Chun-gang, FU Yu-kun, SUN Han-wen, DONG Liang-liang, ZHU Xiao-hua. Review of key technical principles of multi-stage segmented fracturing sleeve [J]. Journal of Physics: Conference Series, 2020, 1486: 072053.

[2] ZHANG Yi, FENG Xiao-hui, HUANG Qiu-yan, LI Ying-ju, YANG Yuan-sheng. Enhancing mechanical properties and degradation performance of Mg−0.8wt.%Ca alloy by directional solidification [J]. Transactions of Nonferrous Metals Society of China, 2023, 33(2): 409−421.

[3] XI Guo-qiang, MOU Yu, MA Yan-long, ZHAO Xu-han, XIONG Ju, MA Kai, WANG Jing-feng. Effect of volume fraction of 18R-LPSO phase on corrosion resistance of Mg−Zn−Y alloys [J]. Transactions of Nonferrous Metals Society of China, 2023, 33(2): 454−466.

[4] LI Feng, CHENG Wei-li, YU Hui, WANG Hong-xia, NIU Xiao-feng, WANG Li-fei, LI Hang, HOU Hua. Corrosion behavior and mechanical properties of extruded low-alloyed Mg−0.5Bi−0.5Y−0.2Zn alloy [J]. Transactions of Nonferrous Metals Society of China, 2023, 33(3): 743−754.

[5] DAI Chao-neng, WANG Jing-feng, PAN Yuan-lang, MA Kai, PENG Yin-hong, REN Jie, WANG Ye, WANG Dan-qian, WANG Jin-xing, MA Yan-long. Tailoring the microstructural characteristic and improving the corrosion rate of Mg−Gd− Ni alloy by heat treatment with different volume fraction of LPSO phase [J]. Corrosion Science, 2023, 210: 110806.

[6] ZHANG Lei, ZHANG Shuai-jie, OUYANG Kang-xin, ZHOU Yi-huan, HUANG H, XU Pian. Microstructure and mechanical properties of Mg−Er−Cu/Ni/Zn alloys with long period stacking ordered phases [J]. Advanced Engineering Materials, 2021, 23(10): 2100368.

[7] WANG J, LI T, LI H X, MA Y Z, ZHAO K N, YANG C L, ZHANG J S. Effect of trace Ni addition on microstructure, mechanical and corrosion properties of the extruded Mg−Gd−Y−Zr−Ni alloys for dissoluble fracturing tools [J]. Journal of Magnesium and Alloys, 2021, 9(5): 1632−1643.

[8] DAI Chao-neng, WANG Jing-feng, PAN Yuan-lang, MA Kai, PENG Yin-hong, WANG Ye, WANG Dan-qian, RAN Chun-hua, WANG Jin-xing, MA Yan-long. Enhanced corrosion rate for Mg−XEr−1.6Ni alloys with high Er content by regulating the second phase via short-time low-temperature heat treatment [J]. Corrosion Science, 2023, 220: 111227.

[9] MA Kai, LIU Shi-jie, DAI Chao-neng, LIU Xiu-ying, REN Jie, PAN Yuan-lang, PENG Yin-hong, SU Chen, WANG Jing-feng, PAN Fu-sheng. Effect of Ni on the microstructure, mechanical properties and corrosion behavior of MgGd$_1$Ni$_x$ alloys for fracturing ball applications [J]. Journal of Materials Science & Technology, 2021, 91: 121−133.

[10] HAN Zhen-hua, ZHANG Kai, YANG Jun, WEI Ran, ZHANG Chang-jun. Effects of volume fraction of Ni-containing LPSO phase on mechanical and corrosion properties of Mg−Gd−Ni alloys [J]. Materials and Corrosion, 2019, 70(3): 537−548.

[11] DAI Chao-neng, PEI San-lue, MA Kai, WANG Ye, WANG Dan-qian, WANG Jin-xing, MA Yan-long, WANG Jing-feng. Rapid corrosion rates and high mechanical properties of as-extruded Mg−Er−Ni alloys by introducing LPSO and γ′ phases [J]. Journal of Materials Research and Technology, 2023, 24: 6246−6263.

[12] LIU Jian-ing, BIAN Dong, ZHENG Yu-feng, CHU Xiao, LIN Yu-lin, WANG Ming, LIN Ze-feng, LI Mei, ZHANG Yu, GUAN Shao-kang. Comparative in vitro study on binary Mg−RE (Sc, Y, La, Ce, Pr, Nd, Sm, Eu, Gd, Tb, Dy, Ho, Er, Tm, Yb and Lu) alloy systems [J]. Acta Biomater, 2020, 102: 508−528.

[13] ZHANG L, ZHANG S J, XU P, HUANG H. Effects of substitution of Cu with Ni on microstructure and mechanical properties of Mg−Er−Cu alloy [J]. Journal of Materials Engineering and Performance, 2022, 31(1): 552−559.

[14] DU Xing-hao, WEI Cheng-bin, WU Bao-lin, HONG Min, XIA Yu-hang, LI Wan-peng. A high-performance Mg−Er−Zn−Zr alloy with low Er/Zn mass ratio [J]. Journal of Central South University, 2015, 22(11): 4123−4127.

[15] NIE Yu-jin, DAI Jian-wei, LI Xuan, ZHANG Xiao-bo. Recent developments on corrosion behaviors of Mg alloys with stacking fault or long period stacking ordered structures [J]. Journal of Magnesium and Alloys, 2021, 9(4): 1123−1146.

[16] WU S Z, QIAO X G, ZHENG M Y. Ultrahigh strength Mg−Y−Ni alloys obtained by regulating second phases [J]. Journal of Materials Science and Technology, 2020, 45: 117−124.

[17] JIA Lin-yue, DU Wen-bo, FU Jin-long, WANG Zhao-hui, LIU Ke, LI Shu-bo, DU Xian. Obtaining ultra-high strength and ductility in a Mg−Gd−Er−Zn−Zr alloy via extrusion, pre-deformation and two-stage aging [J]. Acta Metallurgica Sinica (English Letters), 2021, 34(1): 39−44.

[18] WANG X W, WANG W, CHEN W, CHEN D M. Effects of Indium on corrosion behavior of Mg−Al−Cu alloy [J]. Materials Characterization, 2021, 177: 111157.

[19] FENG Bao-jing, LIU Guo-nan, YANG Pei-xu, HUANG Sen-sen, QI Dong-qing, CHEN Peng, WANG Cheng-duo, DU Jiang, ZHANG Shao-jun, LIU Jin-hui. Different role of second phase in the micro-galvanic corrosion of WE43 Mg alloy in NaCl and Na$_2$SO$_4$ solution [J]. Journal of Magnesium and Alloys, 2022, 10(6): 1598−1608.

[20] LI Xue-wu, YU Qing-yuan, CHEN Xi, ZHANG Qiao-xin. Microstructures and electrochemical behaviors of casting magnesium alloys with enhanced compression strengths and decomposition rates [J]. Journal of Magnesium and Alloys, 2023, 11(4): 1213−1223.

[21] LIU Qu, CHEN Gao-qiang, ZENG Shen-bo, ZHANG Shuai, LONG Fei, SHI Qing-yu. The corrosion behavior of Mg−9Al−xRE magnesium alloys modified by friction stir processing [J]. Journal of Alloys and Compounds, 2021, 851: 156835.

[22] MA Liang, LI Wei-jie, ZHU Shi-jie, WANG Li-guo, GUAN Shao-kang. Corrosion inhibition of Schiff bases for Mg−Zn−Y−Nd alloy in normal saline: Experimental and theoretical investigations [J]. Corrosion Science, 2021, 184: 109268.

[23] WANG Xue-jian, CHEN Zong-ning, GUO En-yu, LIU Xue-qin, KANG Hui-jun, WANG Tong-min. The role of Ga in the microstructure, corrosion behavior and mechanical properties of as-extruded Mg−5Sn−xGa alloys [J]. Journal of Alloys and Compounds, 2021, 863: 158762.

[24] SUN Yue-hua, WANG Ri-chu, PENG Chao-qun, CAI Zhi-yong. Microstructure and corrosion behavior of as-extruded Mg−xLi−3Al−2Zn−0.2Zr alloys (x = 5, 8, 11 wt.%) [J]. Corrosion Science, 2020, 167: 108487.

[25] CAO Fang-fang, DENG Kun-kun, NIE Kai-bo, KANG Jin-wen, NIU Hao-yi. Microstructure and corrosion properties of Mg−4Zn−2Gd−0.5Ca alloy influenced by multidirectional forging [J]. Journal of Alloys and Compounds, 2019, 770: 1208−1220.

[26] ZHANG Tao, SHAO Ya-wei, MENG Guo-zhe, CUI Zhong-yu, WANG Fu-hui. Corrosion of hot extrusion AZ91 magnesium alloy: I—relation between the microstructure and corrosion behavior [J]. Corrosion Science, 2011, 53(5): 1960−1968.

[27] NIU Hao-yi, DENG Kun-kun, NIE Kai-bo, WANG Cui-ju, LIANG Wei, WU Yu-cheng. Degradation behavior of Mg−4Zn−2Ni alloy with high strength and high degradation rate [J]. Materials Chemistry and Physics, 2020, 249: 123131.

[28] ZHONG Shi-yu, ZHANG Ding-fei, WANG Yong-qin, CHAI

Sen-sen, FENG Jing-kai, LUO Yu-lun, HUA Jian-rong, DAI Qi-min, HU Guang-shan, XU Jun-yao, JIANG Bin, PAN Fu-sheng. Microstructures, mechanical properties and degradability of Mg−2Gd−0.5(Cu/Ni) alloys: A comparison study [J]. Journal of Materials Science & Technology, 2022, 128: 44−58.

[29] MA Kai, WANG Jing-feng, PENG Yin-hong, DAI Chao-neng, PAN Yuan-lang, WANG Ye, WANG Dan-qian, WANG Jin-xing, MA Yan-long, PAN Fu-sheng. Achieving high strength and rapid degradation in Mg−Gd−Ni alloys by regulating LPSO phase morphology combined with extrusion [J]. Journal of Magnesium and Alloys, 2024, 12(6): 2312−2326.

[30] ZHANG X, KAIRY S K, DAI J, BIRBILIS N. A closer look at the role of nanometer scale solute-rich stacking faults in the localized corrosion of a magnesium alloy GZ31K [J]. Journal of the Electrochemical Society, 2018, 165(7): C310−C316.

[31] DAI Chao-neng, WANG Jing-feng, PAN Yuan-lang, MA Kai, PENG Yin-hong, REN Jie, WANG Ye, WANG Dan-qian, WANG Jin-xing, MA Yan-long. Achieving exceptionally high strength and rapid degradation rate of Mg−Er−Ni alloy by strengthening with lamellar γ' and bulk LPSO phases [J]. Journal of Materials Science and Technology, 2024, 168: 88−102.

[32] GERASHI E, ALIZADEH R, LANGDON T G. Effect of crystallographic texture and twinning on the corrosion behavior of Mg alloys: A review [J]. Journal of Magnesium and Alloys, 2022, 10(2): 313−325.

[33] LIU Y H, ZHANG Z R, WANG J, LI Y, LI H X, JIA L Y, WANG J H, ZHANG J S. A novel Mg−Gd−Y−Zn−Cu−Ni alloy with excellent combination of strength and dissolution via peak-aging treatment [J]. Journal of Magnesium and Alloys, 2023, 11(2): 720−734.

[34] XIE Jin-shu, ZHANG Jing-huai, ZHANG Zhi, YU Zi-jian, XU Zhi-hao, WANG Ru, FANG Da-qing, ZHANG Xiao-bo, ZHANG Xiao-ru, WU Rui-zhi. Corrosion mechanism of Mg alloys involving elongated long-period stacking ordered phase and intragranular lamellar structure [J]. Journal of Materials Science and Technology, 2023, 151: 190−203.

[35] WANG Kui, WANG Jing-feng, HUANG Song, DOU Xiao-xu, WANG Jin-xing, WANG Cun-long. Formation of an abnormal texture in Mg−Gd−Y−Zn−Mn alloy and its effect on mechanical properties by altering extrusion parameters [J]. Materials Science and Engineering: A, 2022, 831: 142270.

[36] XIA Xiang-sheng, ZHANG Kui, MA Ming-long, LI Ting. Microstructures and strengthening mechanisms of Mg−8.2Gd−4.6Y−1.5Zn−0.4Zr alloy containing LPSO, β' and γ type phases [J]. Journal of Rare Earths, 2020, 38(10): 1119−1125.

[37] LUO Shi-feng, WANG Nan, WANG Yan, CHEN Jie-ming, QIN He, KONG Song, BAI Tong, LU Wen-jie, XIAO Lei, MA Xin-kai, YANG Xin-yu, ZHANG Jiu-xing. Texture, microstructure and mechanical properties of an extruded Mg−10Gd−1Zn−0.4Zr alloy: Role of microstructure prior to extrusion [J]. Materials Science and Engineering: A, 2022, 849: 143476.

[38] ZHOU Yu-cheng, LIU Cheng, LUO Qun, LI Qian. Enhancing strength and ductility of low-cost rare earth Mg−5Y−Ni alloy containing LPSO phase fabricated via multi-pass rolling based on dislocation regulation and grain refinement [J]. Materials Characterization, 2022, 193: 112288.

[39] WANG Peng-yue, WANG Bing-yu, WANG Cheng, WANG Jin-guo, MA Chen-yi, LI Jia-sheng, ZHA Min, WANG Hui-yuan. Design of multicomponent Mg−Al−Zn−Sn−Bi alloys with refined microstructure and enhanced tensile properties [J]. Materials Science and Engineering: A, 2020, 791: 139696.

通过调控 Er 含量实现挤压态 Mg−Er−Ni 合金力学性能和降解速率的协同提升

代朝能 [1,2]，裴三略 [2]，王 叶 [2]，王自红 [2]，王金星 [2]，麻彦龙 [3]，王敬丰 [1,2]

1. 重庆大学 化学化工学院，重庆 401331；
2. 重庆大学 材料科学与工程学院 国家镁合金材料工程研究中心，重庆 400044；
3. 重庆理工大学 材料科学与工程学院，重庆 400054

摘　要：通过控制 Er 含量，研究了挤压态 Mg−xEr−1.6Ni 合金(x=17，12 和 9.5，质量分数，%)力学性能和降解速率的协同提升机理。结果表明，随着 Er 含量的降低，第二相的总含量和分布基本不变，而第二相类型从主要由 LPSO 相向 LPSO 相与 γ' 相共存转变。与高 Er 含量合金(Mg−17Er−1.6Ni)相比，低 Er 含量合金(Mg−9.5Er−1.6Ni)的拉伸屈服强度(TYS)提高了 22.3%，降解速率提高了 51.5%。力学性能的提高主要源于在较低 Er 含量下形成的 γ' 相，该相能够抑制动态再结晶过程，进而细化晶粒，通过第二相和晶界强化来提高合金的 TYS。同时，较细晶粒和 γ' 相既能提供更多腐蚀位点，又能抑制耐蚀 Er_2O_3 腐蚀产物膜的形成，从而加速合金的腐蚀。

关键词：Mg−Er−Ni 合金；力学性能；降解速率；γ' 相

(Edited by Wei-ping CHEN)